Spin diffusion in fullerene-based devices: Morphology effect

Tho D. Nguyen, Fujian Wang, Xiao-Guang Li, Eitan Ehrenfreund, and Z. Valy Vardeny

Phys. Rev. B **87**, 075205 — Published 19 February 2013

DOI: 10.1103/PhysRevB.87.075205

Spin diffusion in fullerene-based devices; morphology effect

Tho D. Nguyen[1*], Fujian Wang[1&], Xiao-Guang Li[2], Eitan Ehrenfreund[1,3], Z. Valy Vardeny[1#]

[1]*Department of Physics & Astronomy, University of Utah, 115 South 1400 East, Salt Lake City, Utah 84112, USA*

[2]*Hefei National Laboratory for Physical Sciences at Microscale, Department of Physics, University of Science and Technology of China, Hefei 230026, People's Republic of China*

[3]*Physics Department and Solid State Institute, Technion-Israel Institute of Technology, Haifa 32000, Israel*

Abstract

The buckminsterfullerene C_{60} molecules are composed of ~99% naturally abundant ^{12}C carbon atoms having spinless nucleus and thus zero hyperfine interaction. Therefore it was assumed that the spin diffusion length in C_{60}-based spin-valves is large. We fabricated spin-valves based on C_{60} and studied the magnitude of the giant magneto-resistance (GMR) as a function of bias voltage, temperature and C_{60} layer thickness. Surprisingly, we found that GMR first increases as the C_{60} layer thickness increases, reaching a maximum at ~35 nm, then exponentially decreases with thickness from which we extracted a small spin diffusion length of ~12 nm at 10 K. From our data we obtain two important conclusions. First, morphology related disorder that originates from the C_{60} nano-crystalline grains embedded into an amorphous phase of C_{60} is responsible for an unusual spin diffusion process that results in short spin diffusion length. Second, we identify the main spin relaxation dynamics in the fullerene to be the grain boundaries in which spin-orbit coupling is enhanced by the local electric field.

* Present address: Department of Physics & Astronomy, University of Georgia, Athens, GA 30602, USA

& Present address: Department of Physics & Astronomy, University of Iowa, Iowa City, Iowa 52242, USA

To whom correspondence should be addressed; e-mail: val@physics.utah.edu

I. Introduction

Spintronics utilizes the electron's spin degree of freedom in addition to its charge in electronic devices for advanced approaches to information storage and processing[1]. For efficient spintronics devices it is necessary to achieve spin *injection, detection and manipulation* of spin polarized carriers[2]. Organic semiconductors (OS) have recently become the center of attention in the spin-tronics community, because of the presumed long spin relaxation time, and the additional functionality of these materials such as electroluminescence. The prototype organic spintronics device, namely the organic spin-valve (SV) is based on an organic semiconductor spacer placed in between two ferromagnetic (FM) electrodes having different coercive fields, where the magneto-resistance (MR) changes upon sweeping the magnetic field, B[3, 4]. When the active layer shows electroluminescence then a spin-organic light emitting device can be fabricated[5]. Organic semiconductors are composed of light elements that are supposed to possess weak spin-orbit coupling (SOC) leading to small spin relaxation rates[6, 7]. Indeed, giant MR (GMR) has been measured in OSV devices based on small molecule and polymer spacers, both as thick films and thin tunnel junctions[4, 6-13]. Clear proof of spin *injection* into organic spacer was also provided by muon spin rotation[14] and two photon photoemission spectroscopy[15].

The hyperfine interaction (HFI) has been recently shown to play a significant role in limiting the spin diffusion length in polymer organic SV devices[12, 16]. In addition, the SOC, which has been a useful tool in manipulating the injected spin aligned carriers in inorganic spintronics devices[17], should be considered[18] also in organic SV devices, in spite of the light atoms comprising the organic materials. In fact, the weak SOC is the reason that organic spintronics has been attractive in the first place[2].

The buckeyball C_{60} molecule is composed of 60 carbon atoms (see Fig. 1d inset), of which 98.9% are the natural abundant ^{12}C isotope having spinless nucleus, and thus zero HFI; and ~1.1% ^{13}C isotope having nuclear spin ½ with estimated HFI constant of ~0.2 μeV[19]. Therefore the HFI constant averaged on the 60 carbon atoms of natural C_{60} molecule should be ~3 neV, which is too small to play any significant role in magneto-transport. It has therefore been assumed that the spin diffusion length in fullerene-based spin valve (SV) devices is relatively large. However since the C_{60} molecule is strongly curved, significant hybridization may occur between the π and σ electrons, and this might enhance the SOC. Recent calculations[20] estimated the SOC in C_{60} to be less than 1 μeV; this is a relatively small value but is larger than the HFI in this molecule, and thus may be a key factor in limiting the spin diffusion length in C_{60} spin-valves.

A 9% MR at room temperature has recently been reported[21] for a C_{60} SV device with thickness d=5 nm, that diminishes to 5.5% at d=28 nm. The spin transport mechanism was attributed[21] to a multi-step tunneling process through the C_{60} buckyballs. In another recent report[22] on C_{60} SV devices, a 13% GMR at T=15 K and d=25 nm was obtained. From the thickness dependent GMR(d) it was estimated[22] that the spin diffusion length is several tens of nanometers, comparable to other organic SV devices.

In this work we studied GMR of C_{60} based SVs and correlated the results to the morphology of the active layer. We found that evaporated C_{60} films contain micro-crystalline domains of diameter $D\approx10$ nm in size, that grow in density and size with the film thickness, d, followed by saturation at $d\approx40$ nm. The measured GMR(d) response shows a peculiar maximum at $d_0\approx35$ nm that obscures spin diffusion length measurements. Nevertheless, we determined the spin diffusion length, λ_{C60} for C_{60} SV devices with $d>d_0$; we obtained $\lambda_{C60}\approx12$ nm at 10 K that strongly depends on the temperature. We discuss the unusual GMR(d) response in terms of the unusual film nano-morphology coupled with the ensuing energy disorder. In particular we identify the main spin relaxation in the fullerene to occur at the grain boundaries, where the SOC may be enhanced due to the strong local electric field.

II. <u>Experimental</u>

The fullerene SVs were fabricated using C_{60} evaporated films as spacers with various thicknesses in between two FM electrodes[3] namely $La_{0.67}Sr_{0.33}MnO_3$ (LSMO) [bottom electrode, FM_1], and cobalt (Co) [top electrode, FM_2]. The LSMO films having thickness of ~200 nm and area of 5×5 mm^2, were grown epitaxially on <100> oriented $SrTiO_3$ substrates at 735° C using dc magnetron sputtering technique, with Ar and O_2 flux in the ratio of 1:1. The films were subsequently annealed at 800° C for ~10 hours before slow cooling to room temperature[13]. The LSMO films were patterned using standard photolithography and chemical etching techniques. LSMO is stable against oxidation, and thus the films were cleaned and reused *multiple times* as substrates without visible degradation[3]. Following the LSMO substrate cleaning using toluene and chloroform, we evaporated the C_{60} layer in an evaporation chamber with base pressure of $5x10^{-7}$ torr. Subsequently, we deposited a thin (5 - 7 nm) Co film capped by an aluminium (Al) film using a shadow mask. The obtained active device area was typically about 0.2 x 0.4 mm^2. C_{60} is quite robust against Co clusters penetration, and this eliminated the problem of an 'ill defined' film thickness encountered before using OSV with Tris(8-hydroxyquinolinato)aluminum (Alq_3) organic interlayer[3]. The C_{60} film thickness d was controlled by a quartz crystal thickness monitor, and calibrated against measurements using thickness profilometry methods (KLA Tencor). C_{60} SV devices with various d were measured and compared at several bias voltages, V, and temperatures, T. Typical device resistance was in the range of 5 kΩ (for d=20 nm) to 500 kΩ (for d=90 nm).

The C_{60} SV devices were placed on a cold finger end in vacuum in a closed-cycle helium refrigerator. The SV GMR response was measured in the temperature range of 10 to 300 K using the 'four probe' method, while varying an external in-plane magnetic field. The magnetization properties of the FM electrodes were measured by the magneto-optic Kerr effect (MOKE). From these measurements we determined typical low temperature coercive fields for the unassembled electrodes B_{c1}~4.5 mT and B_{c2}~16.5 mT, for the LSMO and Co (covered by 15 nm C_{60}) films, respectively.

Ttransmission electron microscopy (TEM) images of clusters in C_{60} films were studied using a FEI TEM machine operating at 80 kV. For measuring the nano-crystalline (NC) grain size and density as a function of the film thickness we evaporated several films on Formvar carbon films placed on copper grids, with the same overall effective film thickness normalized to a 90 nm film. For films with small d values we measured several films put together in series separated by ~2 nm organic thin films (Alq_3) to preserve the effective d. For the x-ray diffraction (XRD) pattern we used a CuK_α X-ray machine with λ=0.154 nm; each scattering pattern was collected for 6 hours to attain good signal to noise (S/N) ratio. For obtaining the various Bragg bands from the C_{60} crystalline grains we removed from the film scattering pattern the scattering pattern of the substrate, which was measured separately. The Bragg scattering bands were translated into crystal plane-spacing, d_{hkl}, using the Bragg relation $2d_{hkl}\sin 2\theta_{hkl}=\lambda$, where $2\theta_{hkl}$ is the scattering angle for the hkl planes with $d_{hkl}=a/(h^2+k^2+l^2)^{½}$,where a is the cubic lattice parameter and hkl are the cubic Miller indices. The NC grain size, D, was estimated using the Scherrer's equation[23]:

$$D = 0.9\lambda/\Delta_{2\theta}\cdot\cos\theta, \qquad (1)$$

where $\Delta_{2\theta}$ is the full-width-at half maximum of the (111) Bragg band at $2\theta_{111}=10.6°$. For the dependence of D on the film thickness we evaporated C_{60} on a glass substrate and kept constant the XRD scattering S/N ratio by using the same technique as described above for the TEM measurements, namely keeping constant a normalized effective d of ~155 nm.

III. Experimental Results

A. C_{60} film Morphology

Figure 1a is a TEM image of a d=90 nm thick C_{60} film grown on a thin metal grid. The TEM image clearly shows the formation of domains having higher C_{60} density than that of the surrounding matrix, which we thus identify as NC grains. From the TEM image we estimate an average grain size, D<30 nm. We found, however, that the grain size and their number density *increase* with the film thickness. The NC domains formed in the film are also clearly seen in the phase atomic force microscope (AFM) image of a 50 nm thick C_{60} film grown on LSMO substrate, as shown in Fig. 1b. In addition, the AFM study shows good film roughness of ~0.9 nm that is crucial for fabricating high quality C_{60} SV devices.

Figure 1c shows the grazing incidence XRD pattern from a 155 nm thick C_{60} film deposited on a glass substrate, using the CuK_α X-ray line at λ=0.154 nm. Four Bragg scattering bands are clearly seen above the scattering background that is due to the glass substrate. C_{60} is known to crystallize in a fcc Bravais lattice (BL) structure with lattice constant, $a\approx1.42$ nm (Ref. [24]); we therefore analyze the obtained Bragg scattering bands using this natural BL structure. We could fit the three obtained Bragg bands at large scattering angle, 2θ as originating from fcc NC grains in the film with a=1.41 nm having (hkl) Miller indices of (111), (220) and (311) at $2\theta_{hkl}$=10.8°, 17.8° and 20.9°, respectively. We note, however, that the (200) Bragg band, which is allowed in fcc

BL structures, is not present in the XRD pattern (Fig. 1c). This is due to the room temperature rotational motion of the C_{60} molecules around one of their central axes, which renders their scattering symmetry to that of spheres; this enhanced symmetry eliminates the (200) band[24]. In addition, we also estimated the average NC grain size D~10 nm from the full width at half maximum (FWHM), $\Delta_{2\theta}$ of the (111) Bragg band (Fig. 1c inset) using Eq. 1. In contrast, the Bragg band at 2θ=6.6°, denoted "disordered cubic" (*dc*), cannot be accounted for using the most abundant fcc BL structure. We note, however, that there is another C_{60} crystalline structure which is somewhat disordered but stable at high temperatures. This structure has a distorted fcc BL with a=1.36 nm (Ref. [24]). We thus identify the obtained *dc* band as due to (100) Bragg scattering band coming from a fcc BL with a=1.34 nm, that is allowed here due to the disorder resulting from the relatively small NC grain size in the film.

Figure 1d shows the film thickness dependence of the grain size and intensity, A, under the (111) Bragg scattering band, which were measured on a variety of C_{60} films having normalized thickness. It is clearly seen that both D and *A increase with the thickness d*, followed by a saturation above d_s≈45 nm. The increase of the film crystallinity with d complicates the analysis of spin transport and spin diffusion measurements in C_{60} SV devices at small d values, because it may influence carrier mobility that should be larger in the crystalline domains. This, in turn increases the device GMR with d (at small d) due to the expected increase in the spin diffusion length of the injected carriers for C_{60} SV devices fabricated with d≤40 nm (see below).

B. Giant magneto-resistance measurements of C_{60} spin valves

We used C_{60} SV devices in which the fullerene film was sandwiched in between LSMO and Co as the two FM electrodes having different coercive fields (Fig. 2a). These FM electrodes have high nominal spin injection polarization degree, P_1(LSMO)≈98% that is strongly temperature dependent above ~150K (see Fig. 2d, inset), and P_2(CO)≈30% that is essentially temperature independent in the temperature range up to 300 K; but its sign depends on the environment[13, 25]. Since $B_{c1} \neq B_{c2}$, then it is possible to switch the relative magnetization directions of the FM electrodes in the SV device between parallel (P) and anti-parallel (AP) alignments upon sweeping B; whereby the device resistance, R is dependent on the relative magnetization orientations. The SV device resistance was measured using the four-probe technique at constant current. Figure 2b shows typical GMR hysteresis response of a C_{60} SV fabricated with the layer configuration LSMO/C_{60}(35nm)Co/Al, measured at various temperatures. It is seen that R(AP)<R(P), i.e. a sign opposite to that of inorganic spin-valves, but in agreement with many other organic SV devices based on LSMO and Co electrodes[3, 4]. The 'turn-on' and 'turn-off' GMR(B) response are quite sharp, similar to the best spin-valve devices[4, 11]. Bobbert *et al*. (BWOKW)[26] attributed the sharpness of the 'turn on' and 'turn off' GMR response in organic SV devices to the HFI of the organic interlayer, being sharper for smaller HFI constant. This model is in agreement with our results, since the HFI in C_{60} film is indeed very small, and this leads to a superior GMR response. In addition, we also see (Fig. 2b) that the coercive fields B_{c1} and B_{c2} decrease strongly with the temperature; this is in agreement with our MOKE measurements (not shown here). In general, both B_{c1} and B_{c2} are much larger for the C_{60} SV than in many other organic SV devices based on LSMO and Co FM electrodes[3, 12]. We do not exactly know the reason for this behavior, but it is conceivable that the coercive fields depend on the specific organic interlayer. When R(AP)<R(P) the maximum GMR value, $[\Delta R/R]_{max}$ (or MR_{SV}) is given by the ratio: $MR_{SV}=[R(P)-R(AP)]/R(AP)$. We notice that MR_{SV} decreases with temperature (Fig. 2b); however, the temperature decrease is not as steep as in other organic SV devices[3, 4].

Figure 2c shows the bias voltage dependence of $MR_{SV}(V)$ at various temperatures. First, we note that $MR_{SV}(V)$ response is rather symmetric about V=0. Second, it is not as steep as in other reported organic SV devices[4, 12]; this may indicate a superior contact surface between the C_{60} film and the two FM electrodes. In addition, it is clear that $MR_{SV}(V)$ response is less steep at elevated temperatures, and this is good news for Organic Spintronics. From the weaker $MR_{SV}(T)$ and $MR_{SV}(V)$ responses we conclude that C_{60}-based SV have *excellent qualities*. Indeed, we found that such devices are sufficiently stable that we could readily measure the GMR hysteresis loop also at room temperature, with MRsv ~0.16% at V=200 mV reaching 0.3% at V<5 mV (Ref. [27]); we note, however, that a 9% MR_{SV} value at room temperature was reported[21] in C_{60} SV having the configuration Co/AlO_x/C_{60}(5nm)/Py, where Py denotes permalloy, $Fe_{80}Ni_{20}$. The obtained MRsv in those devices was interpreted[21] as due to tunneling MR rather than GMR that involves spin transport through the C_{60} layer. The flatter MRsv(V) response with increasing temperature (Fig. 2c) shows that it cannot be entirely due to a decrease in the polarization degree P_1, or P_2 with V, as suggested before[3, 6].

We also plot in Fig. 2d the temperature dependence of MRsv at various V's extracted from Fig. 2c. It is clearly seen that although MRsv(T) response decreases with increasing T, it does not follow the moderate temperature decrease of the LSMO magnetization, M(T) that is shown in Fig. 2d (inset). In addition, MRsv(T) response is clearly voltage dependent (Fig. 2c), and the response is symmetric about V=0. These characteristic properties show that MRsv(V,T) response cannot be explained solely by the dependence of the FM injecting capability through $P_1(V,T)$ of the LSMO electrode[6], because it is difficult to understand that $P_1(V)$ (or $P_2(V)$) is completely symmetric for injecting either electrons or holes. We therefore conclude that the decrease in MRsv at high T and V reveals an *intrinsic spin relaxation mechanism* which reduces the spin diffusion length at high temperature and/or electric field ($|V|$/d; symmetric about V=0), as measured in Alq_3 films[14], and discussed for Alq_3 SV devices[28].

Next, we tried to estimate λ_{C60} from the SV device performance at various C_{60} thickness at V=100 mV, as shown in Fig. 3a for T=10 K. For these measurements we used the same LSMO substrate but different interlayer thickness, since LSMO is relatively stable in air, and its spin injection properties were found to be quite robust[3]. According to the modified Jullière formula[3, 29] when MR_{SV} <<100% (see Figs. 2b,e) it should be a monotonic decreasing function of d :

$$MR_{SV} \approx 2P_1P_2\exp[-d/\lambda_{C60}], \qquad (2)$$

where λ_{C60} is the spin diffusion length in the fullerene interlayer. *Surprisingly*, the obtained $MR_{SV}(d)$ first *increases* with d, reaches a maximum at d_0≈35 nm, and decreases thereafter with the C_{60} interlayer thickness for $d>d_0$. This rather peculiar behavior may be explained taking into account the film morphology at increasing d. As discussed above, the film crystallinity increases with d at small d-values, but saturates at d_S≈45 nm, approximately where $MR_{SV}(d)$ starts decreasing (Fig. 3a). The less disordered the C_{60} layer becomes with increasing d (at $d<d_0$), the higher is the charge carrier mobility, thereby increasing λ_{C60} [26]. We thus conclude that the unusual $MR_{SV}(d)$ increase at small d arises from the increase in the spin diffusion length because of the increase in carrier mobility with d. Since the increase in film crystallinity saturates at $d_S \sim d_0$, then $\lambda_{C60}(d)$ also saturates, i.e. $\lambda_{C60}(d>d_0) \approx \lambda_{C60}(d=d_0) \equiv \lambda_0$, resulting in an exponential decrease of $MR_{SV}(d)$ for $d>d_0$ that shows a constant $\lambda_{C60} \equiv \lambda_0$. In order to extract λ_0 from our GMR measurements we fit $MR_{SV}(d)$ decrease for devices with $d>d_0$ using Eq. (2) obtaining λ_0≈12 nm (Fig. 3a).

Surprisingly, this value is smaller than λ_S reported for Alq_3 (~45 nm, Ref. [3]), and λ_S obtained in π-conjugated polymers (~30 nm, Ref. [12]), even though the HFI is much smaller in C_{60}. The HFI in C_{60} is too weak to explain such a small λ_{C60}; we thus conclude that other spin relaxation mechanisms limit the spin diffusion length in the C_{60} film.

C. Discussion

(i) The short C_{60} spin diffusion length. We propose that carrier spin dynamics in C_{60} film is composed of both hopping in the disordered C_{60} matrix and ballistic transport in the C_{60} NC crystalline grains. Injected carriers inside the grain may bounce back and forth many times before escaping into the disordered matrix that surrounds the grains, resulting in an overall reduced spin diffusion length that is related with spin relaxation mechanism at the grain boundaries. The obtained $\lambda_{C60}\approx 12$ nm (for $d>d_0$) is very similar in magnitude to the average grain size D (~10 nm), and this lends support for this hypothesis. We note that if not for the relatively small grain size, λ_{C60} might have been much larger because the intrinsic spin relaxation mechanism is indeed weak in this material. As mentioned above, the HFI is unlikely to play an important role in C_{60} because 99% ^{12}C with zero nuclear spin; thus we consider the SOC as the most dominant spin relaxation mechanism in the fullerene, similar as in graphene (which is in fact another carbon allotrope). Carbon is a light atom with relatively small atomic SOC of the order of ~6 meV[30]; this is too large to explain our results. However, since the orbital angular momentum is mostly quenched for π-orbital electron or hole carriers in planar organic molecules[31], then the atomic SOC is expected to be substantially reduced to less than ~0.1 μeV in carbon based organic molecules, including graphene and possibly also C_{60} (Ref. [20]).We showed above that C_{60} films are composed of NC grains of various sizes and shapes. Consequently, upon the application of a bias voltage, substantial electric fields may form at the grain boundaries that, in turn, may enhance the SOC through the Stark effect[20, 30]. Nevertheless, given the applied voltage employed here, we expect the SOC to be quite small, giving rise to relatively long spin relaxation times. Another boundary spin relaxation mechanism may be due to finite surface spin flip probability, as suggested recently for mesoscopic systems[32]. Therefore, it is conceivable that the obtained short spin diffusion length in C_{60} SV devices is limited by the grain size dimension. Although the effective SOC gives rise to relatively long spin relaxation times, carriers inside the grain bounce back and forth many times before escaping the grain, thereby decreasing the spin diffusion length. It is thus expected that SV devices based on smooth, mostly crystalline C_{60} would have much larger spin diffusion length.

(ii) The MR non-monotonic thickness dependence. As the thickness increases from d=20 nm, the C_{60} film becomes more crystalline, and the disordered regions shrink. BWOKW[26] introduced a model in which the spin diffusion in disordered organic semiconductors is controlled by a combination of incoherent carrier hopping together with coherent spin evolution around a local effective magnetic field. BWOKW considered disordered organic matrix with random site energies distributed having a Gaussian density of states with a width σ, and local effective magnetic field caused by the vector addition of a random hyperfine field combined with the static external applied magnetic field. We believe that this model is not necessarily limited to random local fields caused by the HFI, but is equally applicable to random local fields that originate from other mechanisms; e.g., the SOC. According to BWOKW, λ_S increases as the disorder is reduced; this is mainly due to the increase in carrier mobility when the layer becomes less disordered. BWOKW therefore concluded[25] that the bottleneck mechanism that limits the spin diffusion length, λ_S, is not the spin relaxation time (which may be long) but rather the waiting time between consecutive hops.

Using this model we may explain the non-monotonic $MR_{SV}(d)$ response displayed in Fig. 3a as follows. At d_1=20 nm (the thinnest layer studied here), where the disorder in the film is relatively large, the parameter $\lambda_{C60}(d_1)$ is small (~8-9 nm); as d increases above d_1 the disorder in the film decreases and in turn λ_{C60} increases up to a maximum value reached at $d=d_0$. For $d>d_0$ the film disorder stays put and the energy distribution width σ does not decrease anymore with d, and thus λ_{C60} remains unchanged at $\lambda_0 \approx \lambda_{C60}(d_0)$. Consequently, $MR_{SV}(d)$ for $d>d_0$ follows the dependence expected by Eq. (2) with fixed spin diffusion length parameter, λ_0. Fitting $MR_{SV}(d)$ for $d>d_0$ (Fig. 3a) with Eq. (2), we find $MR_{SV}(d>d_0)=MR_0\exp(-d/\lambda_0)$ with $\lambda_0 \approx 12$ nm and $MR_0=0.6$. According to BWOKW model the spin diffusion length λ_S increases dramatically even with a slight decrease of σ; e.g., at an electric field $F \approx \sigma/ea$ (a is the lattice constant), $\lambda_S/a \sim(\sigma/k_BT)^{-\alpha}$, with $\alpha \approx 4$ for σ in the range $3 \leq \sigma/k_BT \leq 6$ (deduced from Fig. 1b in Ref. [26]). We therefore conclude that even a slight variation in the disorder width, σ, brings about a large change in the spin diffusion length. Assuming that Eq. (2) holds also for $d<d_0$ with d-dependent disorder-limited spin diffusion length, we have $\lambda_{C60}(d)=\ln(MR_0/MR_{SV}(d))$, with $MR_0=0.6$ as above; this dependence is shown in Fig. 4 (blue symbols) as the ratio $\lambda_{C60}(d)/\lambda_0$ vs. d. Using the relation between λ_S and σ obtained from BWOKW model, we also plot in Fig. 4 the ratio $\sigma(d)/\sigma(d>d_0)$ (red symbols) vs. d. It is clearly seen that a mild ~40% variation in σ is sufficient to explain the unusual $MR_{SV}(d)$ functional dependence shown in Fig. 3a.

(iii) The MR temperature dependence. For the MR_{SV} temperature dependence we consider the Elliott-Yafet (EY) mechanism[33, 34], which is most suitable for hopping transport. According to EY, the spin randomization rate is due to carrier scattering events, and therefore is inversely proportional to the momentum relaxation time, τ. Since τ decreases at elevated temperatures, then the spin relaxation rate increases and consequently λ_S decreases at high temperatures[14, 28]. We note that if not for the EY mechanism, then λ_S would have increased with the temperature, since the carrier diffusion constant in organic semiconductors is higher at elevated temperatures[28]. But such an increase is contrary to the obtained MRsv(T) shown in Fig. 2d, where MRsv(T) sharply decreases with temperature, steeper than the decrease of LSMO magnetization M(T) (see Fig. 2d, inset). Since MRsv(V) analysis presented above showed that it is determined by a bulk spin scattering mechanism in the C_{60} layer rather than the LSMO P_1 value, it is reasonable to assume that MRsv(T) response is substantially influenced by the temperature dependence of the relevant spin relaxation mechanism in the organic layer. To understand MRsv(T) we extract the dependence of the spin relaxation rate on temperature by dividing MRsv(T) by $P_1(T)$ response (Eq.(2)), assuming that $P_1(T)$ is represented by M(T) of the LSMO electrode. M(T) shown in Fig. 2d (inset) can in fact be very well fit by a Brillouin function, $B_J(T/T_c)$ with J=5/2 and T_c=307 K. We thus obtain $\lambda_0(T)$ using the relation $\lambda_0(T)=d/\ln(MR_0\, B_{5/2}(T/T_c)\,/MRsv(T))$ (with MR_0=0.6) from the data in Figs. 2c,d; this is shown in Fig. 3b (symbols). Interestingly, the obtained $\lambda_0(T)$ at V=0, can be very well fit with an activated function: $[1/\lambda_0(T)-1/\lambda_0(0)]\propto\exp(-\Delta/k_BT)$, with Δ=16±3 meV (solid line, Fig. 3b). The obtained thermally activated behavior indicates a parallel behavior of the spin relaxation rate.

D. Summary

We have studied the GMR in C_{60} based spin valves, in which the hyperfine interaction is nearly absent and does not play any important role in limiting the spin diffusion. Surprisingly, we found that the GMR value first increases as the C_{60} layer thickness increases, reaching a maximum at ~35 nm, then exponentially decreases with thickness showing a small spin diffusion length of ~12 nm at 10 K. We show that morphology related disorder which originates from the combination of C_{60} crystalline grains embedded within an amorphous phase of C_{60} is responsible for the unusual GMR thickness dependence and short spin diffusion length. We then explain the obtained spin diffusion length in C_{60} films as due to a spin relaxation mechanism at the grain boundary, which we identify to be SOC enhanced by the local electric fields at the NC grain boundaries.

Acknowledgements
We thank Y. Zheng for help with XRD. This work was supported in part by the Department of Energy, Grant No. 04-ER46109 (ZVV; C_{60} SV device fabrication and GMR measurements); the NSF Grant No. DMR-1104495, (ZVV and TDN; the x-ray measurements and analysis of C_{60} films); the NSFC and National Basic Research Program of China, Grant 2006CB922005 (XGL; the LSMO substrates); the Israel Science Foundation, ISF 472/11 (EE; the spin diffusion process); and the US-Israel Binational Science Foundation, BSF 2010135 (EE and ZVV; SV discussions and manuscript writing).

References

1. S. A. Wolf, D. D. Awschalom, R. A. Buhrman, J. M. Daughton, S. von Molnar, M. L. Roukes, A. Y. Chtchelkanova and D. M. Treger, Science **294** (5546), 1488-1495 (2001).
2. W. J. M. Naber, S. Faez and W. G. van der Wiel, J Phys D Appl Phys **40** (12), R205-R228 (2007).
3. Z. H. Xiong, D. Wu, Z. V. Vardeny and J. Shi, Nature **427**, 821-824 (2004).
4. V. A. Dediu, L. E. Hueso, I. Bergenti and C. Taliani, Nat Mater **8**, 707-716 (2009).
5. T. D. Nguyen, E. Ehrenfreund and Z. V. Vardeny, Science **337**, 204-209 (2012).
6. F. J. Wang, C. G. Yang, Z. V. Vardeny and X. G. Li, Phys Rev B **75**, 245324 (2007).
7. S. Pramanik, C. G. Stefanita, S. Patibandla, S. Bandyopadhyay, K. Garre, N. Harth and M. Cahay, Nat Nanotechnol **2** (4), 216-219 (2007).
8. L. E. Hueso, I. Bergenti, A. Riminucci, Y. Q. Zhan and V. Dediu, Adv Mater **19**, 2639-+ (2007).

9. T. S. Santos, J. S. Lee, P. Migdal, I. C. Lekshmi, B. Satpati and J. S. Moodera, Phys Rev Lett **98** (1) (2007).
10. N. Tombros, C. Jozsa, M. Popinciuc, H. T. Jonkman and B. J. van Wees, Nature **448** (7153), 571-U574 (2007).
11. V. Dediu, L. E. Hueso, I. Bergenti, A. Riminucci, F. Borgatti, P. Graziosi, C. Newby, F. Casoli, M. P. De Jong, C. Taliani and Y. Zhan, Phys. Rev. B **78**, 115203 (2008).
12. T. D. Nguyen, G. Hukic-Markosian, F. J. Wang, L. Wojcik, X. G. Li, E. Ehrenfreund and Z. V. Vardeny, Nat Mater **9**, 345-352 (2010).
13. C. Barraud, P. Seneor, R. Mattana, S. Fusil, K. Bouzehouane, C. Deranlot, P. Graziosi, L. Hueso, I. Bergenti, V. Dediu, F. Petroff and A. Fert, Nat Phys **6**, 615-620 (2010).
14. A. J. Drew, J. Hoppler, L. Schulz, F. L. Pratt, P. Desai, P. Shakya, T. Kreouzis, W. P. Gillin, A. Suter, N. A. Morley, V. K. Malik, A. Dubroka, K. W. Kim, H. Bouyanfif, F. Bourqui, C. Bernhard, R. Scheuermann, G. J. Nieuwenhuys, T. Prokscha and E. Morenzoni, Nat Mater **8**, 109-114 (2009).
15. M. Cinchetti, K. Heimer, J. P. Wustenberg, O. Andreyev, M. Bauer, S. Lach, C. Ziegler, Y. L. Gao and M. Aeschlimann, Nat Mater **8**, 115-119 (2009).
16. B. R. Gautam, T. D. Nguyen, E. Ehrenfreund and Z. V. Vardeny, Phys. Rev. B **85**, 205207 (2012).
17. L. Y. Yang, J. Orenstein and D. H. Lee, Phys. Rev. B **82** (15) (2010).
18. Z. G. Yu, phys. Rev. Letters **106**, 106602 (2011).
19. M. Karplus and G. K. Fraenkel, J. Chem. Phys. **35**, 1312-1323 (1961).
20. D. Huertas-Hernando, F. Guinea and A. Brataas, Phys. Rev. B **74**, 155426 (2006).
21. M. Gobbi, F. Golmar, R. Llopis, F. Casanova and L. E. Hueso, Adv Mater **23**, 1609-1613 (2011).
22. R. Lin, F. Wang, M. Wohlgenannt, C. He, X. Zhai and Y. Suzuki, Synthetic Met **161**, 553-557 (2011).
23. A. Patterson, Phys. Rev. **56**, 978-982 (1939).
24. P. A. Heiney, J. E. Fischer, A. R. McGhie, W. J. Romanow, A. M. Denenstein, J. P. McCauley Jr, A. B. Smith and D. E. Cox, Phys Rev Lett **66** (22), 2911-2914 (1991).
25. P. Ruden, Nat Mater **10** (1), 8-9 (2011).
26. P. A. Bobbert, W. Wagemans, F. W. A. van Oost, B. Koopmans and M. Wohlgenannt, Phys. Rev. Letters **102** (2009).
27. Z. V. Vardeny and F. J. Wang, Synthetic Met **160** (3-4), 210-215 (2010).
28. S. Bandyopadhyay, Phys. Rev. B **81**, 153202 (2010).
29. M. Julliere, Phys. Letters A **54** (3), 225-226 (1975).
30. H. Min, J. E. Hill, N. A. Sinitsyn, B. R. Sahu, L. Kleinman and A. H. MacDonald, Phys Rev B **74**, 165310 (2006).
31. D. Beljonne, Z. Shuai, G. Pourtois and J. L. Bredas, J. Phys. Chem. A **105**, 3899-3907 (2001).
32. G. Mihajlovic, J. E. Pearson, S. D. Bader and A. Hoffmann, Phys. Rev. Letters **104**, 237202 (2010).
33. R. J. Elliott, Phys. Rev. **96**, 266-279 (1954).
34. Y. Yafet, in *Solid State Physics*, edited by F. Seitz and D. Turnbull (Academic, New York, 1963), Vol. 14, pp. 1-98.

Figure Captions

FIG. 1 (color on line) Morphology characterization of C_{60} films grown by evaporation. (a) Electron transmission microscope image of a 90 nm thick C_{60} film grown on a metal grid. The darker domains are due to C_{60} crystalline grains ~20-40 nm in diameter. (b) Typical AFM image (shown in phase mode) of a C_{60} film; the C_{60} clusters are clearly evident. (c) X-ray diffraction (XRD) pattern using CuK_α line vs. the scattering angle, 2θ measured off a 155 nm thick C_{60} film grown on a glass substrate. The inset shows the four pronounced Bragg scattering peaks after removing the scattering background due to the glass substrate; they are denoted *dc* (disordered cubic), and three (hkl) Miller indices of the fcc Bravais lattice from the crystalline grains. (d) The C_{60} NC grain size and the area under the (111) Bragg scattering peak in the XRD pattern (see inset in (c)), plotted vs. the film thickness, *d*. Note the grain size initial increase with *d*, followed by saturation at d>~45 nm.

FIG. 2 (Color on line) Magnetic field response of C_{60}-based SV. (a) Schematics of a C_{60} SV device and the magneto-resistance measurement configuration. The C_{60}-based SV device consists of two ferromagnetic electrodes (namely LSMO and cobalt) and a C_{60} interlayer of thickness, *d*. (b) Typical GMR loops of a LSMO/C_{60}(30nm)/Co/Al SV device measured at bias voltage V=100 mV and four different temperatures, as shown. **(c)** The GMR magnitude, MR_{SV} vs. V at various temperatures up to 240 K, as obtained from the I-V device characteristics at AP and P magnetization directions of the FM electrodes. The solid lines through the data points (for V>0) are fits to guide the eyes. (d) The $MR_{SV}(T)$ response at various V's extracted from (c); the lines serve as guide to the eyes. Inset: The LSMO magnetization vs. T, and its fit using the Brillouin function, $B_J(T/T_c)$ with J=5/2 and T_c=307 K.

FIG. 3 (Color on line) (a) MR_{SV} of C_{60}-based SV devices measured at V=10 mV and T=10 K vs. the interlayer C_{60} thickness, *d*, showing a pronounced maximum at d_0~35 nm. The line through the data points for $d>d_0$ shows a fit of MR_{SV} to Eq. (2) with spin diffusion length, λ_0=12 nm. (b) The temperature dependence of λ_0 at $V\approx0$ extracted from the fits to the data shown in Fig. 2(b), corrected for the temperature dependence of the LSMO magnetization, M(T) [see text]. The line through the data points is a fit with a thermally activated spin diffusion, $[1/\lambda_0(T)-1/\lambda_0(0)]\propto\exp(-\Delta E/k_BT)$, with $\Delta E=16\pm3$ meV.

FIG. 4. (Color on line) Blue square symbols: thickness dependence of the disorder limited spin diffusion length, $\lambda_{C60}(d)$, plotted as the ratio λ_{C60}/λ_0, with λ_0=12 nm. Red round symbols: The

thickness dependence of the extracted disorder width, σ, plotted as the ratio σ/σ_{d0}, where σ_{d0} is the energy disorder width for $d \geq d_0$. The solid lines serve as guide to the eyes.

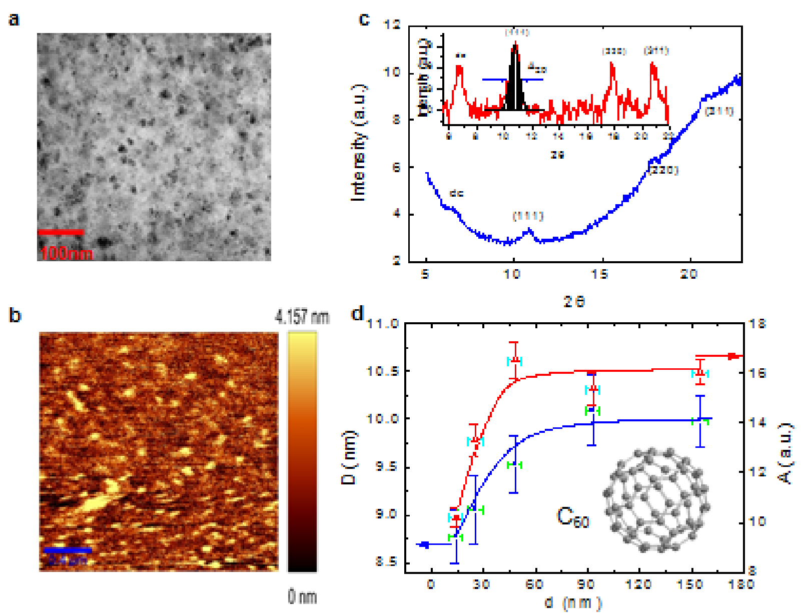

FIG. 1

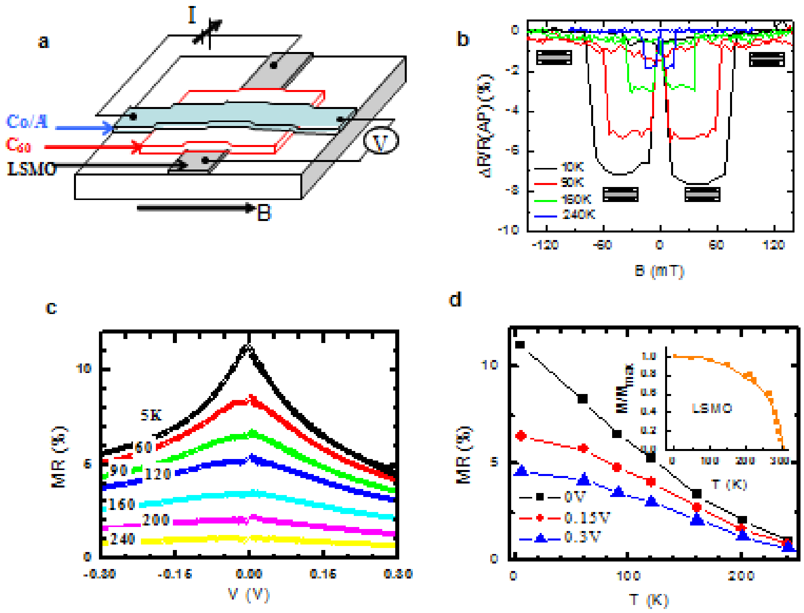

a
I
Co/Al
C_{60}
LSMO
V
B
b
ΔR/R(AP) (%)
10K
90K
160K
240K
B (mT)
c
MR (%)
5K
60
90
120
160
200
240
V (V)
d
MR (%)
0V
0.15V
0.3V
T (K)
LSMO

FIG. 2

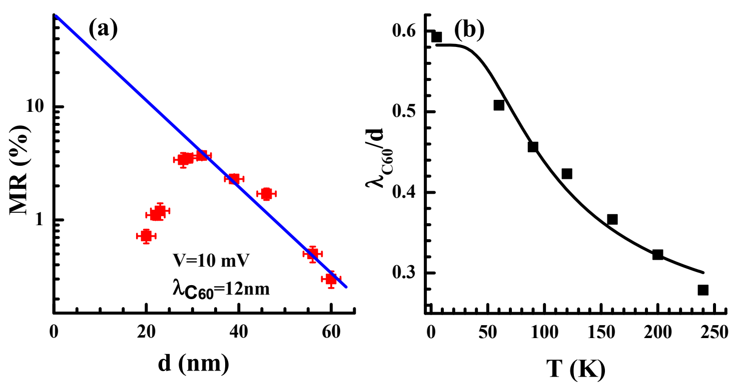

(a)
MR (%)
V=10 mV
λ_{C60}=12nm
d (nm)
(b)
λ_{C60}/d
T (K)

FIG. 3

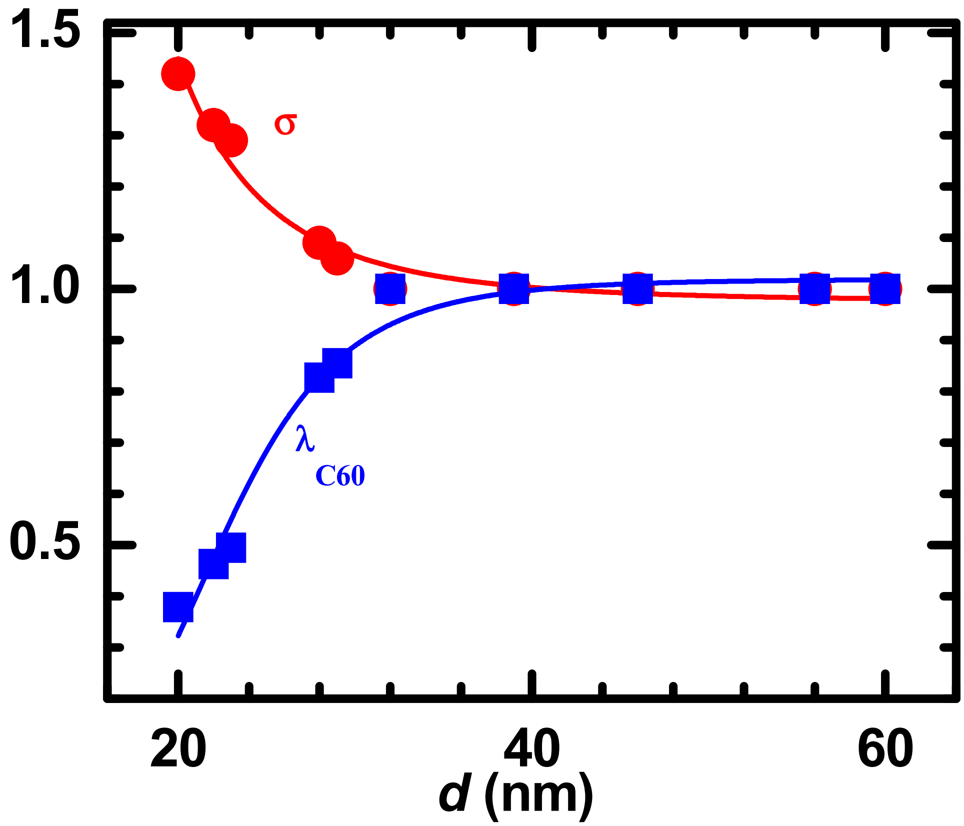

FIG. 4